Autoionizing Rydberg wave packets

F. Robicheaux[1] and W. T. Hill III[2]

[1]*Department of Physics, Auburn University, Auburn, Alabama 36849*
[2]*Institute for Physical Science and Technology, University of Maryland, College Park, Maryland 20742*
(Received 26 March 1996)

In this paper we present some of the general features of autoionizing Rydberg wave packets. We assume the wave packets are generated by a short, *perturbative* laser pulse that excites the electronic wave function to a coherent distribution of final state energies in the autoionizing regime. We describe a possible experiment for generating and detecting these autoionizing wave packets. A physical effect we call ''cresting of a wave packet'' is described. Several calculations for Ba are presented. The cresting of the ejected wave packets should be observable for this atom. Several other effects may also be of interest: the suppression of particular wave packets, the angular distribution associated with a wave packet, different decay rates in different directions, and the systematic variation of angular distribution with the delay time. [S1050-2947(96)08210-8]

PACS number(s): 42.50.Vk, 34.80.Kw, 31.30.Jv, 31.10.+z

I. INTRODUCTION

The advent of transform limited, short laser pulses has allowed Rydberg states to be studied in the time domain. These short pulses excite electrons *coherently* over a range of energies, creating a time-dependent wave packet [1–6]. A wave packet is a *wave function* made up of a coherent superposition of stationary states; i.e., the coefficients of the stationary states have well defined phases relative to each other. Most previous discussions of Rydberg wave packets have involved bound electrons. The focus of this paper will be on autoionizing Rydberg states and the physics that can be probed by a time-dependent detection of the electrons ejected into the continua degenerate with these states. Experimental examples of wave packet studies above an ionization threshold are those of Broers *et al.* [7] and Fielding *et al.* [8]. These were multichannel experiments because the alkali-metal atom was in an electric field; the core couples together the parabolic coordinate channels that are uncoupled in hydrogen. We consider the interesting physics of multichannel wave packets for open shell atoms not in an electric field. For our studies, the lowest order effect involves at least two coupled channels so the formulation we present is based on a multichannel description of the final state function.

Alber and Zoller [9] presented a review of many aspects of the ''laser excitation of electronic wave packets in Rydberg atoms.'' The main effort was on the description of the Rydberg wave packet while it was bound to the atom. Henle *et al.* [10] gave a theoretical development of wave packets for multichannel systems including the possibility for ionization; that paper discussed the motion of the wave packet when bound to the ion. Fielding [11] recently presented a calculation of ''Rydberg electron wave packet dynamics in molecular hydrogen'' which involves a realization of the work of Henle *et al.* [10] for a real molecular system. One purpose of this paper is to call attention to the interesting wave packet dynamics for packets that have been ejected from atoms.

The majority of the work presented to date discusses probing the behavior of the wave packet with a second laser pulse [12,13]. Since electronic transitions are induced through dipole operators, the second laser probes the wave packet near the nucleus (electrons absorb photons most efficiently near the nucleus) but is restricted by selection rules and transition moments. For autoionizing packets, these restrictions can be removed by direct detection of the electrons ejected from the atom. Lankhuijzen and Noordam [14] have detected the electrons ejected into the continuum by rubidium Rydberg wave packets in an electric field. It is not necessary to employ external fields to eject electrons for multichannel atoms. When a Rydberg series is degenerate with a continuum (autoionizing Rydberg states), the electrons that are naturally ejected from the atom can be detected directly with high temporal resolution. Since the quasibound electron can only exchange energy with core degrees of freedom when it is near the core, the electrons are ejected into the continuum in packets which reflect the time dependence of the electron amplitude near the nucleus. The ejected wave packets can be detected at large distances from the atom. As with Refs. [10,11], multichannel dynamics must be incorporated at a basic level; therefore our theoretical study will be based on multichannel quantum defect theory (MQDT) [15]. This method of detecting the Rydberg wave packet complements the probe laser technique since the amplitude for ejection into the electron continuum does not depend on dipole operators but does depend on electron amplitudes near the core. We will show that the motion of the wave packet in the continuum embodies intrinsically interesting features not present when the packet is probed by a second laser.

This paper presents the basic formulas for describing the creation and detection of Rydberg wave packets in the ionization continuum. We present calculations for Ba to demonstrate the effect and describe a possible experimental realization. We identify some atomic transitions for which experiments can be carried out and interesting effects that may be expected. A property of Rydberg wave packets, temporary reverse dispersion or cresting of the continuum wave packet, is described. Several interesting effects related to the angular distribution of the ejected wave packets will be described. Finally, we freely speculate about interesting aspects of this problem that could be measured. Atomic units are used throughout this paper except where explicitly noted.

II. BASIC THEORETICAL FORMULATION

In the basic formulation, we assume that the energy-dependent atomic parameters can be obtained. In particular, we assume that the threshold energies and the short-range S-matrix and dipole matrix elements can be calculated. The most promising atoms for the proposed experiments appear to be the heavy alkaline earths (Ca, Sr, and Ba). There is excellent agreement between calculated and experimental photoionization cross sections which implies the theoretical parameters that we need for our time-dependent calculations will be available. Accurate calculated cross sections have been obtained for Ca [16,17], Sr [18,19], and Ba [20,21].

It is most convenient to work with the ψ^- type scattering functions since the wave packets representing the outgoing electron can be most easily obtained from this type of function. In a superposition of ψ_{Ej}^- functions of different energy but same channel index, j, you naturally obtain outgoing waves at positive times only in channel j. The ψ^+ type scattering functions could be used but then the analysis would be much more complicated because of the outgoing waves in several channels. At the total electronic energy E, the ψ^- functions in the open channels have the form

$$\psi_{Ej'}^- = \tfrac{1}{2}\mathcal{A}\sum_j \ \Phi_j\{[f_{Ej}(r)+ig_{Ej}(r)]\delta_{jj'}$$
$$+[f_{Ej}(r)-ig_{Ej}(r)](S^\dagger)_{jj'}\}/r \qquad (1)$$

when r is larger than the distance where the continuum electron interacts with the core. This is not the usual ψ^- function [e.g., Ref. [22] Eq. (29) or Ref. [23] Eq. (4.27)] because the Coulomb wave phase shift has not been removed; we will account for this phase shift at a later stage in the calculation. The distance over which this form of the wave function does not apply is extremely small on a macroscopic scale, usually less than 10–100 a.u. The Φ_j are the channel functions which represent the part of the wave function for all of the electronic degrees of freedom except the radial motion of the ionized electron. $S^\dagger$ is the Hermitian conjugate of the physical S matrix which can be obtained from the short-range S matrix using MQDT. The antisymmetrization operator $\mathcal{A}$ has been included purely for formal purposes since the outer electron does not overlap the core electrons where the form (1) is valid. At large distances

$$f_{Ej}(r)\pm ig_{Ej}(r)\rightarrow \mp i\sqrt{\frac{2}{\pi k_j}}\exp[\pm i\phi_{Ej}(r)]$$

$$\phi_{Ej}(r)=k_j r+\frac{1}{k_j}\ln(2k_j r)-\frac{\ell_j\pi}{2}$$
$$+\arg[\Gamma(\ell_j+1-i/k_j)], \qquad (2)$$

where $k_j=\sqrt{2(E-E_j)}$ with E_j the core energy, E the total electronic energy, and ℓ_j the orbital angular momentum of the continuum electron in the jth channel. In atomic units, k_j is the velocity of the electron escaping in channel j. Finally, an important property of the ψ_{Ej}^- functions is that they are energy normalized: $\langle\psi_{Ej}^-|\psi_{E'j'}^-\rangle=\delta(E-E')\delta_{jj'}$ where $\langle\,|\,\rangle$ means integration over the spatial coordinates of all of the electrons and dot products of the spin vectors.

We assume that the wave packets are generated by perturbative excitation from an initial state of the atom with a well defined energy using a pulse of laser light. In what follows we will choose linear polarization for the laser to simplify the formulas in the derivation. After Eq. (9), we describe how to generalize to other polarizations. The wave function is a solution of the Schrödinger equation with the form

$$i\frac{\partial}{\partial t}\Psi=H_A\Psi+ZF(t)\cos\omega t\Psi, \qquad (3)$$

where H_A is the time-independent atomic Hamiltonian and Z is the sum of the z coordinates of all of the electrons (only the dipole interaction of the atom with the laser has been retained). The $F(t)$ is the time-dependent amplitude of the laser pulse and ω is the strongest frequency of the laser pulse. The form of the electric field, $F(t)\cos\omega t$, assumes the light source is coherent. We will assume $F(t)$ is a smooth function which peaks at $t=0$. The Schrödinger equation (3) gives a semiclassical description of the dynamics since the electric field from the laser is treated as a classical entity. Squeezed light might give coherences in the electron wave packets in addition to the ones described below.

We obtain the wave function using eigenstates of H_A as a representation,

$$\Psi=A_I(t)\psi_I e^{-iE_I t}+\sum_{j'}\ \int dE'\,\psi_{E'j'}^- A_{E'j'}^-(t)\exp(-iE't), \qquad (4)$$

where

$$H_A\psi_I=E_I\psi_I, \quad H_A\psi_{Ej}^-=E\psi_{Ej}^-, \qquad (5)$$

where E_I is the initial state energy and E is the energy of the state ψ_{Ej}^-. This representation is possible because the eigenstates of H_A form a complete and orthonormal set. In all that follows, we assume the laser interacts with the atom *perturbatively*; this allows us to set $A_I(t)=1$. If we substitute the representation of the wave function from Eq. (4) into the Schrödinger equation (3) and project ψ_{Ej}^- onto this equation, we find the $A_{Ej}^-(t)$ are solutions of

$$i\frac{\partial}{\partial t}A_{Ej}^-(t)=\langle\psi_{Ej}^-|Z|\psi_I\rangle F(t)e^{-i(E_I-E)t}\cos\omega t, \qquad (6)$$

with the condition $A_{Ej}^-(-\infty)=0$. The $A_{Ej}^-(t)$ can be found by integrating both sides of Eq. (6) with respect to t. In all of our applications, we are interested in the wave function at very large distances from the atom well after the pulse has turned off, therefore we are only interested in $A_{Ej}^-(\infty)$ [$A_{Ej}^-(t)$ for t greater than the turn off time equals $A_{Ej}^-(\infty)$] which have the form

$$A_{Ej}^-(\infty)=-\frac{i}{2}\langle\psi_{Ej}^-|Z|\psi_I\rangle\mathcal{F}(E-E_I-\omega), \qquad (7)$$

where

$$\mathcal{F}(\varepsilon)=\int_{-\infty}^{\infty}dt F(t)e^{i\varepsilon t}. \tag{8}$$

The term proportional to $\mathcal{F}(E-E_I+\omega)$ in Eq. (7) is extremely small and has been set to zero because $\mathcal{F}(\varepsilon)$ is strongly peaked around $\varepsilon=0$. Removing the term proportional to $\mathcal{F}(E-E_I+\omega)$ is the rotating wave approximation. Before substituting Eq. (7) into Eq. (4), we can analyze the structure of A_{Ej}^- to gain insight into the behavior of the wave packet in the ionization continuum.

Equation (4) with Eq. (7) is the basis for all of the theoretical development in this paper; the rest of this paper explores the implications of these equations for the dynamics of multichannel wave packets. We would like to stress two important assumptions that entered our derivation. First, the laser-atom interaction is perturbative so we do not need to worry about depletion of the initial state $[A_I(t)=1]$, Rabi oscillations, or other multiphoton effects. Second, we assume that the light source is a coherent pulse in time; to the extent possible, the laser pulse is transform limited. For our derivation, this means that the different frequency components of the laser have well specified relative phases that do not drastically vary from one pulse to the next. If $\mathcal{F}(\varepsilon)$ equaled $|\mathcal{F}(\varepsilon)|\exp[i\delta(\varepsilon)]$ where $\delta(\varepsilon)-\delta(0)$ were unknown phases that varied from one laser pulse to the next in an unknown fashion, it would be necessary to average our results with respect to these phases; this averaging would eliminate the coherences in the wave function, Eq. (4), making the wave packets unobservable.

The easiest piece of A_{Ej}^- to understand is the dependence on angular momentum. If we use the Wigner-Eckhart theorem we can write

$$\langle\psi_{Ej}^-|Z|\psi_I\rangle=(-1)^{J_j-M_j}\begin{pmatrix}J_j & 1 & J_I\\ -M_j & 0 & M_I\end{pmatrix}D_{Ej}^-, \tag{9}$$

where D_{Ej}^- is the reduced dipole matrix element connecting the initial state with ψ_{Ej}^-, J_j (J_I) is the total angular momentum for the jth channel (initial state), and M_j (M_I) is the projection of the total angular momentum on the z axis for the jth channel (initial state). The D_{Ej}^- do not depend on polarization of the light or the magnetic quantum numbers of the initial or final state. If circularly polarized light is used (instead of linear polarization), the 0 in the 3-j symbol is changed to a ±1 (the sign depending on whether right or left circularly polarized light is used). Generalization to mixed polarization is straightforward.

We can further analyze the A_{Ej}^- using ideas from MQDT. Within this framework, the energy dependence in the D_{Ej}^- can be partitioned into pieces that vary rapidly with energy and pieces that vary slowly. In the first stage of applying MQDT, we treat the wave function as if all of the channels were open channels even though some of the channels may be closed. At this stage, all of the wave functions diverge in the closed channels. Of course, these wave functions are not physical because of this divergence. However, they contain important information that allows the construction of the physical wave function. The form of the wave function is similar to that of Eq. (1) except the sum over j includes open and closed channels

$$\psi_{Ej'}^{-(s-r)}=\mathcal{A}\frac{1}{2r}\sum_{j\in o,c}\Phi_j\{[f_{Ej}(r)+ig_{Ej}(r)]\delta_{jj'}$$
$$+[f_{Ej}(r)-ig_{Ej}(r)](\mathcal{S}^\dagger)_{jj'}\}. \tag{10}$$

The $\mathcal{S}$ is the short-range S matrix you obtain by treating all of the channels as open channels. There are corresponding reduced dipole matrix elements which can be written as

$$\mathcal{D}_{Ej'}^-=\langle\psi_{Ej'}^{-(s-r)}||Z||\psi_g\rangle. \tag{11}$$

Although the parameters in Eqs. (10) and (11) are unphysical because of the divergence in the closed channels, the physical wave function, S-matrix, and reduced dipole matrix elements can be obtained by superposing the short-range wave function in order to eliminate the exponential divergence in the closed channels. In matrix notation

$$D_{Eo}^-=\mathcal{D}_{Eo}^- -\mathcal{S}_{oc}[\mathcal{S}_{cc}-\exp(-2i\beta_c)]^{-1}\mathcal{D}_{Ec}^-, \tag{12}$$

$$S_{oo}=\mathcal{S}_{oo}-\mathcal{S}_{oc}[\mathcal{S}_{cc}-\exp(-2i\beta_c)]^{-1}\mathcal{S}_{co}, \tag{13}$$

where the o, c subscripts on the short-range S-matrix or dipole matrix element stand for open, closed channels and $\exp(-2i\beta_c)$ is a diagonal matrix with elements $\exp(-2i\beta_j)$ for the jth closed channel and $\beta_j=\pi(\nu_j-\ell_j)$; the effective quantum number $\nu_j=1/\sqrt{2(E_j-E)}$ with E_j the core electron's energy in channel j. The $[\mathcal{S}_{cc}-\exp(-2i\beta_c)]^{-1}$ is a matrix inversion in general. The advantage of using this formulation hinges on the slow variation with energy of the short-range parameters $\mathcal{D}$ and $\mathcal{S}$. The Rydberg series of resonances and the fast energy dependence arise from the β_j.

If you substitute the form Eq. (12) for the reduced dipole matrix element into Eq. (9) and combine Eqs. (9), (7), and (4) you can obtain the time dependence of the continuum part of the wave function. The function $\mathcal{F}(E-E_I-\omega)$ is a smooth, peaked function near $E=E_I+\omega$. For ease of analytic integration in the discussion below we will choose $\mathcal{F}(\varepsilon)$ to be $F_0\exp(-\alpha\varepsilon^2)$. However, in the numerical calculations the integration in Eq. (4) is executed numerically so this restriction can be easily lifted to incorporate the experimental $\mathcal{F}(\varepsilon)$ in the calculations. The reason for the choice of Eq. (1) for the representation of the wave function becomes apparent when the integration in Eq. (4) is executed. Set $k_j(E)\simeq\bar{k}_j+(E-E_I-\omega)/\bar{k}_j$ [with $\bar{k}_j=k_j(E_I+\omega)$] and integrate with respect to E, the largest contribution from the $f-ig$ part of the wave function is proportional to

$$\int dE \exp\{-i[(E-E_I-\omega)(t+r/\bar{k}_j)]\}\mathcal{F}(E-E_g-\omega)$$
$$\propto F(t+r/\bar{k}_j), \tag{14}$$

which gives an ingoing wave packet at positive r and negative times or wave packets at (unphysical) negative r at positive times. We are interested in the wave function at very large distances and t must be greater than 0, which is the reason for the last equality. Therefore we can calculate the continuum wave at very large r from only the $f+ig$ part of the wave function. This simplification gives

$$\psi_{\text{cont}} = -\frac{1}{\sqrt{8\pi}} e^{-i\bar{E}t} \sum_j \frac{1}{r} \Phi_j (-1)^{J_j - M_j}$$

$$\times \begin{pmatrix} J_j & 1 & J_I \\ M_j & 0 & M_I \end{pmatrix} F_{\max} \xi_j(r,t), \qquad (15)$$

$$\xi_j(r,t) = e^{i\phi_{\bar{E}j}(r)} \int d\varepsilon\, e^{-i\varepsilon t} \frac{\mathcal{F}(\varepsilon)}{F_{\max}} D^-_{\bar{E}+\varepsilon, j}$$

$$\times \exp\{i[\phi_{\bar{E}+\varepsilon, j}(r) - \phi_{\bar{E}, j}(r)]\}/\sqrt{k_j(\bar{E}+\varepsilon)}, \qquad (16)$$

where $\bar{E} = E_I + \omega$, $\phi_{Ej}(r)$ is from Eq. (2), $F_{\max}$ is the maximum of $|F(t)|$, and $\varepsilon = E - \bar{E}$ is a dummy variable which simplifies the numerical integration. (In all that follows, the barred parameters are the parameters evaluated at the energy $E = \bar{E} = E_I + \omega$.) We have tested the second line numerical integration with the full $\psi_{\bar{E}j}$ and with only the $f + ig$ part of the wave function and obtained the same answer to numerical precision. In the experiments that we will consider, the part of the wave function Ψ, Eq. (4), proportional to $\psi_I \exp(-iE_I t)$ is zero at the detector because of the small spatial extent of the initial state.

Equation (15) is the basic formula describing the creation and detection of autoionizing Rydberg wave packets at large distances from the atoms; $5.3 \text{ cm} = 10^9$ a.u. We will focus on the situation where a detector will measure the rate of electrons entering an aperture at a certain distance. The subtleties involved in obtaining the flux (in particular the angular dependence of ψ_{cont} and averaging over unobserved quantum numbers in the initial and final states) are presented in the next section.

III. TEMPORAL CROSS SECTION

The wave function of Eq. (15) is the correct form of the electron wave packet after the electron has left the atom. It is important to determine to what extent this function may be observable. We will consider a simple detector that measures the radial electron flux as a function of time; the flux will depend on the distance to the detector and the direction of the detector with respect to the laser polarization.

One of the simplest measurements that might be practical for this system is of the *rate* of electrons entering a detector at a position $\vec{r}$ relative to the nucleus. If the angular size subtended by the entrance to the detector is small enough, the rate that electrons enter the detector can be simply related to the radial flux of electrons at $\vec{r}$ by dividing the rate by the area subtended by the detector. The quantum mechanical calculation of the radial flux for a one electron function $y(\vec{r},t)$ is written as

$$\frac{1}{2i}\left[y^* \frac{\partial y}{\partial r} - \left(\frac{\partial y^*}{\partial r}\right) y \right] = \text{Im}\left(y^* \frac{\partial y}{\partial r} \right). \qquad (17)$$

In calculating the radial flux for the wave function Ψ, it is not necessary to include the ψ_I part of the function because it does not extend to large distances and is thus zero at the detector. The radial flux from Ψ, $\mathfrak{F}_{\text{rad}}$, equals

$$\mathfrak{F}_{\text{rad}}(\vec{r},t) = \text{Im}\left[\left\langle\!\left\langle \psi_{\text{cont}} \left| \frac{\partial}{\partial r} \right| \psi_{\text{cont}} \right\rangle\!\right\rangle\right], \qquad (18)$$

where the double $\langle\!\langle\ \rangle\!\rangle$ notation means to integrate and trace over all of the core electrons' degrees of freedom and trace over the spin of the outer electron. This averaging procedure is necessary when only the outer electron's flux is measured. If the electron flux were measured simultaneously with some other parameter (e.g., the spin of the outer electron or the energy of the core state), this formula would need to be modified.

In many respects the radial flux is important, partly because it is relatively easy to calculate and measure. However, in some ways it is not useful because simple changes in the electric field profile, $F(t)$, will cause changes in the flux. For profiles with the same shape but different electric field strengths, $F(t) = \alpha F_1(t)$, the radial flux will be proportional to α^2. This suggests defining a fundamental parameter proportional to the radial flux divided by the maximum intensity of the laser field. We choose to define this parameter in such a way that it equals the usual definition of the differential cross section in the limit that the laser pulse is infinitely narrow in frequency (a laser pulse infinitely long in time). The differential photoionization cross section equals the rate of electrons entering a detector divided by the angular size of the detector and the photon flux. This quantity equals the radial electron flux times the distance to the detector squared divided by the photon flux. This leads to the definition of our temporal cross section being

$$\frac{d\sigma(\vec{r},t)}{d\Omega} = \mathfrak{F}_{\text{rad}}(\vec{r},t)r^2/\mathfrak{F}_{\text{max photon}}. \qquad (19)$$

The temporal cross section manifestly has units of area. The maximum in time of $d\sigma(\vec{r},t)/d\Omega$ can be formally shown to become equivalent to the usual photoionization cross section in the limit the laser is monochromatic. We do not present this lengthy derivation. However, a simple physical argument shows this must be true. As the laser becomes monochromatic, maximum photon flux $\mathfrak{F}_{\text{max photon}}$ becomes simply the photon flux and the $\mathfrak{F}_{\text{rad}}(\vec{r},t) \to \mathfrak{F}_{\text{rad}}(\hat{\vec{r}})$. Equation (19) becomes the usual definition of the differential photoionization cross section in this limit. The temporal cross section can be used to determine the rate at which electrons enter a detector.

IV. PROPERTIES OF THE TEMPORAL CROSS SECTION

A. Angular distribution from a specific M_I

In this section, formulas for the differential temporal cross section are derived for the case when the initial state has a specified magnetic quantum number M_I. This situation might occur if the initial state is an excited state of the atom that was populated by a laser with a well defined polarization. For example, the initial state of Ba might be the $6p^2\ {}^3P_J$ states excited by two photons from a laser linearly polarized in the z direction; for this case, $M_I = 0$ even though the J_I could be 0 or 2 depending on the laser frequency. Since the initial state can be strongly aligned, the angular

distribution can have stronger angular dependence than if the initial state has a random distribution of M_I.

The formula for radial flux, Eq. (18), contains averages over unobserved quantum numbers. This averaging is somewhat cumbersome in the usual couplings [24]: (1) jj coupling (where the ℓ of the outer electron is coupled to the spin of the outer electron to give a total angular momentum of the outer electron which is then coupled to the total angular momentum of the core electrons) or (2) jK coupling (where the ℓ of the outer electron is coupled to the total angular momentum of the core to give K, which is then coupled to the spin of the outer electron). Instead of these couplings jQ coupling will be utilized (this was called $J_c J_{cs}$ coupling in Lindsay *et al.* [25]); the total angular momentum of the core is coupled to the spin of the outer electron to give Q, which is then coupled to the orbital angular momentum of the outer electron to give the total angular momentum.

The equation for the radial flux incoherently sums over all of the unobserved quantum numbers; these are all of the quantum numbers not associated with the position of the outer electron. To be specific, a channel j is determined by

the following quantum numbers: n_j (specifies the core state), Q_j (arises from the coupling of the total angular momentum of the n_j core state with the spin of the outer electron), ℓ_j (the orbital angular momentum of the outer electron), J_j (the total angular momentum), and M_j (the projection of the total angular momentum on the z axis). The channel function Φ_j equals

$$\Phi_j = \psi_{n_j}^{core} \sum_{M_q, m} |Q_j M_q\rangle Y_{\ell_j m}(\Omega) \langle Q_j M_q \ell_j m | J_j M_j \rangle, \tag{20}$$

where $|Q_j M_q\rangle$ represents the function where the total angular momentum of the core state, $\psi_{n_j}^{core}$, couples to the spin of the outer electron giving angular momentum Q_j and projection M_q and $\langle Q_j M_q \ell_j m | J_j M_j \rangle$ is the Clebsch-Gordan coefficient that couples together the Q_j and ℓ_j angular momentum to total angular momentum J_j with a z projection M_j. The Clebsch-Gordan coefficient can be written in terms of the 3-j symbol [Eq. (3.7.3) of Edmonds [26]].

The radial flux in Eq. (18) can now be obtained explicitly using Eqs. (15), (18), and (20),

$$\mathfrak{F}_{rad}(\vec{r},t) = \frac{F_{max}^2}{8\pi r^2} \text{Im}\Bigg[\sum_{j,j'} \xi_j^*(r,t)\xi_{j'}'(r,t) \delta_{Q_j Q_{j'}} \delta_{n_j n_{j'}} (-1)^{J_j + J_{j'} + 2Q_j - \ell_j - \ell_{j'}} [J_j, J_{j'}] \sum_{M_q, m, m'} Y_{\ell_{j'} m'}(\Omega) Y_{\ell_j m}^*(\Omega)$$

$$\times \begin{pmatrix} Q_j & \ell_j & J_j \\ M_q & m & -M_j \end{pmatrix} \begin{pmatrix} Q_j & \ell_{j'} & J_{j'} \\ M_q & m' & -M_{j'} \end{pmatrix} \begin{pmatrix} J_j & 1 & J_I \\ -M_j & 0 & M_I \end{pmatrix} \begin{pmatrix} J_{j'} & 1 & J_I \\ -M_{j'} & 0 & M_I \end{pmatrix} \Bigg], \tag{21}$$

where $\xi_{j'}'(r,t) = \partial \xi_{j'}(r,t)/\partial r$ and $[J] = \sqrt{2J+1}$. The zeros in the 3-j coefficients arise from the linear polarization of the laser; these zeros should be changed to ± 1 if the laser is circularly polarized. This expression can be reduced further using relationships for products of $Y_{\ell m}$ and identity relationships for sums of 3-j symbols.

The temporal cross section can now be obtained from the radial flux. The maximum photon flux equals $cF_{max}^2/8\pi\omega$, which will give the temporal cross section as

$$\frac{d\sigma^{(M_I)}(\vec{r},t)}{d\Omega} = \frac{1}{4\pi} \sum_\ell \sigma_\ell^{(M_I)}(r,t) P_\ell(\cos\theta), \tag{22}$$

where $\cos\theta = \hat{\vec{r}} \cdot \hat{\vec{z}}$ and the time-dependent coefficients are independent of all of the magnetic quantum numbers except M_I and the magnetic quantum number from the laser polarization. The time-dependent coefficients are given by

$$\sigma_\ell^{(M_I)}(r,t) = \frac{(2\ell+1)\omega}{c} \sum_{j,j'} \text{Im}[\xi_{j'}'(r,t)\xi_j^*(r,t)] \delta_{Q_j Q_{j'}} \delta_{n_j n_{j'}} (-1)^{J_j + J_{j'} - M_I + Q_j} [\ell_j, \ell_{j'}, J_j, J_{j'}] \begin{pmatrix} J_j & 1 & J_I \\ -M_I & 0 & M_I \end{pmatrix}$$

$$\times \begin{pmatrix} J_{j'} & 1 & J_I \\ -M_I & 0 & M_I \end{pmatrix} \begin{pmatrix} \ell_j & \ell_{j'} & \ell \\ 0 & 0 & 0 \end{pmatrix} \begin{pmatrix} J_j & \ell & J_{j'} \\ -M_I & 0 & M_I \end{pmatrix} \begin{Bmatrix} J_j & \ell & J_{j'} \\ \ell_{j'} & Q_j & \ell_j \end{Bmatrix}. \tag{23}$$

The coefficient $\sigma_0^{(M_I)}(r,t)$ is the total temporal cross section. The angular distribution is determined by the parameters $\sigma_\ell^{(M_I)}(r,t)/\sigma_0^{(M_I)}(r,t)$ where the maximum value of ℓ is $2J_I + 2$; if $J_I = 0$, the only nonzero terms in the sum is $\ell = 0$ and 2. Only even values of ℓ are nonzero in the summation of Eq. (23); this means the angular distribution is symmetric about $\theta = 90°$.

The derivation of the differential temporal cross section mirrors the derivation for the more usual energy-dependent differential cross section (Starace [23]). A difference between this derivation and the more usual one is that the asymptotic Coulomb phase shifts have not been incorporated into the dipole matrix elements. However, the $\exp[i\phi_{\bar{E}j}(r)]$ factor in Eq. (16) is the analog of Coulomb phase shift term in the energy-dependent photoionization cross section.

B. Angular distribution from average M_I

In the preceding section, the angular distribution from a specific M_I state was found. If the initial projection of the total angular momentum on the z axis is completely unknown, then the angular distribution must be obtained by averaging the temporal cross section over the M_I quantum number. This temporal cross section will be

$$\frac{d\sigma^{\mathrm{av}}(\vec{r},t)}{d\Omega}=\frac{1}{2J_I+1}\sum_{M_I=-J_I}^{J_I}\frac{d\sigma^{(M_I)}(\vec{r},t)}{d\Omega}=\frac{1}{4\pi}\sum_{\ell}\sigma_{\ell}^{\mathrm{av}}(r,t)P_{\ell}(\cos\theta),\qquad(24)$$

where the summation is only over $\ell=0$ and 2. The coefficients from Eq. (23) can be used in the average over M_I to obtain

$$\sigma_{\ell}^{\mathrm{av}}(r,t)=\frac{(2\ell+1)\omega}{(2J_I+1)c}\begin{pmatrix}1&1&\ell\\0&0&0\end{pmatrix}\sum_{j,j'}\mathrm{Im}[\xi_{j'}'(r,t)\xi_j^*(r,t)]\delta_{Q_jQ_{j'}}\delta_{n_jn_{j'}}(-1)^{Q_j-J_I}[\ell_j,\ell_{j'},J_j,J_{j'}']\begin{pmatrix}\ell_j&\ell_{j'}&\ell\\0&0&0\end{pmatrix}$$

$$\times\begin{Bmatrix}1&1&\ell\\J_{j'}&J_j&J_I\end{Bmatrix}\begin{Bmatrix}J_j&\ell&J_{j'}\\\ell_{j'}&Q_j&\ell_j\end{Bmatrix}.\qquad(25)$$

Equations (24) and (25) could be used to write the temporal cross section as

$$\frac{d\sigma^{\mathrm{av}}(\vec{r},t)}{d\Omega}=\frac{\sigma_0^{\mathrm{av}}(r,t)}{4\pi}[1+\beta(r,t)P_2(\cos\theta)],\qquad(26)$$

where $-1\leq\beta\leq2$ and $\beta(r,t)=\sigma_2^{\mathrm{av}}(r,t)/\sigma_0^{\mathrm{av}}(r,t)$. This equation is analogous to the usual formula for the differential photoionization cross section. When $\beta\sim2$, the electrons are mainly ejected in the direction of the laser polarization and when $\beta\sim-1$, the electrons are mainly ejected perpendicular to the laser polarization.

The angular distributions presented in these two sections have the same form as the angular distributions for monochromatic light. However, the angular distributions for monochromatic light involve the interference between the electrons directly excited to the continuum and the electrons first excited into autoionizing levels. In the temporal cross section, the wave packets from these two different paths do not overlap in general. Hopefully, the temporal cross section will provide more insight into the atomic dynamics for this reason.

C. Time-dependent radial packets

In this section we explore the structure of the radial part of the wave packets in the ionization continuum. Most of the processes described in this paper have their counterparts in previous studies involving Rydberg wave packets. The reverse dispersion or cresting of ionization wave packets is an interesting new effect.

Before presenting detailed numerical calculations, we will explore the generic behavior of the ionization Rydberg wave packets. To accomplish this goal we will restrict ourselves to one open channel but with any number of closed channels. We first express the dipole matrix element from Eq. (14) as a series expansion of the form

$$D_{Eo}^-=\mathcal{D}_{Eo}^-+\sum_{j\in c}\mathcal{S}_{oj}e^{2i\beta_j}\mathcal{D}_{Ej}^-+\sum_{j,j'\in c}\mathcal{S}_{oj}e^{2i\beta_j}\mathcal{S}_{jj'}e^{2i\beta_{j'}}\mathcal{D}_{Ej'}^-$$

$$+\sum_{j,j',j''\in c}\mathcal{S}_{oj}e^{2i\beta_j}\mathcal{S}_{jj'}e^{2i\beta_{j'}}\mathcal{S}_{j'j''}e^{2i\beta_{j''}}\mathcal{D}_{Ej''}^-\cdots\quad(27)$$

This equation results from the expansion of $[\mathcal{S}_{cc}-\exp(-2i\beta_c)]^{-1}$ in powers of $\mathcal{S}_{cc}$. Each of the terms will contribute different packets to the ψ_{cont}. The packets will have a simple form if they do not overlap and complicated interference patterns otherwise.

To analytically obtain the integral in Eq. (16) to meaningful accuracy, it is necessary to expand all of the exponentiated functions of energy to second order in ε. We assume the function $\mathcal{F}(\varepsilon)$ is strongly peaked near $\varepsilon=0$ so this expansion has meaning. If only the first order terms are kept, the wave packets will not disperse. We do not need to worry about the energy dependence of the $\mathcal{D}^-$, $\mathcal{S}$, and $k^{-1/2}$ (in the normalization of $f+ig$) because their energy dependence is negligible over the width of $\mathcal{F}(\varepsilon)$. The Taylor series expansion of the β_j is appropriate only if the number of Rydberg states in the packet is small compared to the effective quantum number $\bar{\nu}_j$ in that channel. When this condition holds the expansion of β_j is

$$\beta_j\approx\pi\bar{\nu}_j+\pi\bar{\nu}_j^3\varepsilon+\tfrac{3}{2}\pi\bar{\nu}_j^5\varepsilon^2,\qquad(28)$$

where $\bar{\nu}_j=1/\sqrt{2(E_j-E_I-\omega)}$. The radial phase ϕ can be expanded as

$$\phi_o(r)=\phi_o^{(0)}(r)+\varepsilon\phi_o^{(1)}(r)+\frac{\varepsilon^2}{2}\phi_o^{(2)}(r),\qquad(29)$$

where

$$\phi_o^{(0)}(r)=\bar{k}_or+\frac{1}{\bar{k}_o}\ln(2\bar{k}_or)-\frac{\ell_o\pi}{2}$$

$$+\mathrm{Im}[\ln\Gamma(\ell_o+1-i/\bar{k}_o)],\qquad(30)$$

$$\phi_o^{(1)}(r) = \frac{r}{k_o} + \frac{1}{\bar{k}_o^3}\{-\ln(2\bar{k}_o r) + 1 + \mathrm{Re}[\psi(\ell_o + 1 - i/\bar{k}_o)]\},$$

$$(31)$$

$$\phi_o^{(2)}(r) = -\frac{r}{\bar{k}_o^3} + \frac{3}{\bar{k}_o^5}\left\{\ln(2\bar{k}_o r) - \frac{4}{3} - \mathrm{Re}\left[\psi\left(\ell + 1 - \frac{i}{\bar{k}_o}\right)\right]\right\}$$

$$-\frac{1}{\bar{k}_o^6}\mathrm{Im}\left[\psi'\left(\ell + 1 - \frac{i}{\bar{k}_o}\right)\right], \qquad (32)$$

where $\psi(z) = \Gamma'(z)/\Gamma(z)$ and $\bar{k}_o = \sqrt{2(E_I + \omega - E_o)}$ with E_o the core energy for channel o.

If we now assume a Gaussian form for $\mathcal{F}(\varepsilon) = F_0 \exp(-\alpha\varepsilon^2)$, all of the integrals can be obtained analytically. Equations (27)–(32) give

$$\frac{1}{\sqrt{8\pi}}e^{-i\bar{E}t}\int d\varepsilon\, e^{-i\varepsilon t}\mathcal{F}(\varepsilon)D_{\bar{E}+\varepsilon,o}^{-}\frac{1}{\sqrt{k_o(\bar{E}+\varepsilon)}}e^{i\phi_o(r)}$$

$$= \frac{1}{\sqrt{8\bar{k}_o}}e^{i[\phi_o^{(0)}(r) - \bar{E}t]}F_0\left(\mathcal{D}_{Eo}^{-}\frac{1}{\sqrt{w(r)}}\right.$$

$$\times \exp\{-\tfrac{1}{4}[\phi_o^{(1)}(r) - t]^2/w(r)\}$$

$$+ \sum_j \mathcal{S}_{oj}e^{2i\pi\bar{\nu}_j}\frac{1}{\sqrt{w(r) - 3i\pi\bar{\nu}_j^5}}$$

$$\times \exp\{-\tfrac{1}{4}(\phi_o^{(1)} + 2\pi\bar{\nu}_j^3 - t)^2/[w(r) - 3i\pi\bar{\nu}_j^5]\}$$

$$\left.\times \mathcal{D}_{Ej}^{-} + \cdots\right) \qquad (33)$$

where $w(r) = \alpha - i\phi_o^{(2)}(r)/2$. The different terms in this equation can be identified with specific types of processes as will be discussed in the following paragraphs.

The first term in the large parentheses comes from the direct ionization of the atom by the laser. This term has the expected structure being proportional to $\mathcal{D}_{\bar{E}o}^{-}$ with a Gaussian wave packet that reaches position r at time $t = \phi_o^{(1)}(r) = r/\bar{k}_o - \delta t_{\mathrm{Coul}}$ where δt_{Coul} arises because the Coulomb potential increases the velocity of the electron; thus the electron arrives at r sooner than if no potential existed. Another important aspect of the first term is dispersion of the wave packet in the continuum. The full width at half maximum of the absolute value squared for the first term is

$$\Delta t = \sqrt{\frac{2\ln 2}{\alpha}}\{\alpha^2 + [\phi_o^{(2)}(r)/2]^2\} \simeq \tfrac{1}{2}\Delta\omega r/\bar{k}_o^3, \quad (34)$$

where $\alpha = 2\ln 2/\Delta\omega^2$, $\Delta\omega$ is the full width at half maximum of the squared amplitude $|\mathcal{F}(\varepsilon)|^2$, and the last term holds at large distances. The width of the direct ionization wave packet increases linearly with the distance to the detector for large distances. The dispersion of the wave packet in the

continuum is an important effect because it will determine whether the wave packets will be observed as individual packets at the detector.

The second term in the large parentheses of Eq. (33) results from initial excitation of the electron into Rydberg states in channel j with subsequent scattering from the core into the ionization channel. The $\mathcal{D}_{\bar{E}j}^{-}$ gives the amplitude for absorption into channel j, $\exp(2i\pi\bar{\nu}_j)$ gives the amplitude to travel out from the core in channel j and return and scatter from the core, and the $\mathcal{S}_{oj}$ is the amplitude for the electron to scatter from channel j into the open channel during one collision with the core. The peak of the packet reaches the distance r after a time $t = \phi_o^{(1)}(r) + 2\pi\bar{\nu}_j^3 = r/\bar{k}_o - \delta t_{\mathrm{Coul}} + \tau_j^{\mathrm{Ryd}}$ where τ_j^{Ryd} is the period of a Rydberg electron in channel j. These pulses arrive at the detector at τ_j^{Ryd} later than the first pulse. The full width at half maximum is given by

$$\Delta t = \Delta\omega\left[\left(\frac{2\ln 2}{\Delta\omega^2}\right)^2 + [3\pi\bar{\nu}_j^5 + \phi_o^{(2)}(r)/2]^2\right]^{1/2}$$

$$\simeq \Delta\omega\left[\left(\frac{2\ln 2}{\Delta\omega^2}\right)^2 + \left(3\pi\bar{\nu}_j^5 - \frac{r}{2\bar{k}_o^3}\right)^2\right]^{1/2}. \quad (35)$$

Equation (35) indicates a very interesting effect. The width of the packet decreases with r until a distance

$$r_{\mathrm{min}} = 6\pi\bar{k}_o^3\bar{\nu}_j^5 \qquad (36)$$

then increases at larger distances. This distance can be macroscopic; for $\bar{k}_o = 0.27$ a.u. (energy of 1 eV for continuum electron), and $\bar{\nu}_j = 50$, $r_{\mathrm{min}} = 3.9 \times 10^7$ a.u. $= 2.1$ mm.

This is the effect we are calling cresting of the autoionizing wave packets. Mathematically, this effect arises because the term in Eq. (28) quadratic in ε has the opposite sign to the term in Eq. (29) quadratic in ε. Physically this effect occurs because the higher energy part of the Rydberg wave packet takes longer to complete an orbit than the low energy part of the packet; the Rydberg wave packet disperses because the low energy part of the packet gets further and further ahead of the high energy part of the packet. However, once the packet emerges into the continuum the packet has the reverse dispersion; the high energy part of the packet moves faster than the low energy part. The initial dispersion of the Rydberg wave packet is completely reversed at the distance r_{min}.

The cresting of autoionizing wave packets can be quantitatively explained from classical arguments based on the fact that as you increase energy the Rydberg period increases. Suppose you start with two electrons at the origin at $t = 0$, one with energy E and one with energy $E + \Delta E$. The two electrons travel in an elliptic Rydberg orbit for one period at which point they exchange energy with the core and emerge into the continuum. The electron with energy E emerges at time $\tau = 2\pi\bar{\nu}^3$; the electron with energy $E + \Delta E$ emerges at the later time $\tau + \Delta\tau = \tau + 6\pi\bar{\nu}^5\Delta E$. The time it takes for the faster electron to catch the slower electron is $t = \Delta\tau\bar{k}_o/\Delta k = \Delta\tau\bar{k}_o^2/\Delta E = 6\pi\bar{\nu}^5\bar{k}_o^2$ The distance at which the faster electron catches the slower electron is $r = \bar{k}_o t = 6\pi\bar{k}_o^3\bar{\nu}^5$, which is identical to Eq. (36). This distance does not depend on ΔE to lowest order so electrons

with a distribution of energies peaked near E will all reach the distance r_{min} at the same time.

The higher terms in Eq. (33) (represented by $+ \cdots$) give pulses that correspond to n_1 revolutions in channel 1, n_2 revolutions in channel 2, etc. These pulses arrive at times $t = r/k_o - \delta t_{Coul} + \Sigma_j n_j \tau_j^{Ryd}$ These pulses will also exhibit reverse dispersion. They will crest (have minimum width) at a distance

$$r_{min} = 6 \pi \bar{k}_o^3 \sum_j \ n_j \bar{\nu}_j^5 . \tag{37}$$

It is possible (as will be shown in a figure below) that Rydberg wave packets that have dispersed to the extent of strongly overlapping near the nucleus can be distinguished if the distance to the detector is chosen wisely.

D. General aspects of angular distributions

In general, the $\xi_j(r,t)$ functions are calculated numerically from numerical tabulations of dipole matrix elements D_{Ej}^-. In the preceding section we performed a MQDT analysis of the $\xi_j(r,t)$ by expanding the dipole matrix elements and therefore the $\xi_j(r,t)$ functions in powers of the closed-closed part of the short-range S matrix. This leads to an expansion of $\xi_j(r,t)$ in terms of superpositions of wave packets

$$\xi_j(r,t) = \sum_{n_1,n_2,n_3,\ldots=0}^{\infty} C_{n_1 n_2 n_3 \ldots}^j W_{n_1 n_2 n_3 \ldots}(r,t), \tag{38}$$

where n_i is the number of revolutions in channel i, $C_{n_1 n_2 n_3 \ldots}^j$ are constants, and $W_{n_1 n_2 n_3 \ldots}(r,t)$ are wave packets that have been delayed by time $\Sigma_i n_i \tau_i^{Ryd}$ (τ_i^{Ryd} is the Rydberg period in channel i) from the direct ionization pulse $n_1 = 0$, $n_2 = 0$, $n_3 = 0, \ldots$. If several Rydberg series are attached to the same threshold, several of the $W_{n_1 n_2 n_3 \ldots}(r,t)$ will be identical. For example, if channels 1 and 2 have the same threshold then

$$W_{n_1 n_2 n_3 \ldots}(r,t) = W_{n_1 \pm n, n_2 \mp n, n_3 \ldots}(r,t). \tag{39}$$

If a wave packet does not overlap other packets, the $\xi_j(r,t)$ equals a function of r,t that is common to all the channels times a constant that depends on j.

This has a strong effect on the form of the temporal cross section. If a wave packet does not overlap other packets, the angular dependence of the temporal cross section will not vary with time over the width of the packet. For simple Rydberg series (i.e., only degenerate Rydberg wave packets), we can associate an angular distribution with an initial state and the number of revolutions made by the Rydberg wave packet; this is possible because the reverse dispersion always allows a distance where the N revolution packet crests and therefore does not overlap other packets. A point of interest is that for this simple case the angular distribution does not depend on the effective quantum number or period of the Rydberg wave packet.

V. EXPERIMENTAL CONSIDERATIONS

Before looking at the numerical results it is worthwhile summarizing some of the experimental issues that must be considered to realize direct measurement of autoionizing wave packets. An appropriate spectrometer would consist of a picosecond (1–2 ps) light source to excite five to ten autoionizing levels and an electron streak camera to monitor the temporal behavior of the wave packets ejected from the atom. Lankhuijzen and Noordam [14] have recently utilized this basic idea for temporal detection of electrons ejected from Rydberg wave packets generated in rubidium in an external electric field. The simplest design of the electron streak camera would be based on that of an optical streak camera that can be run in a repetitive synchroscan mode but without a photocathode. If cresting of electron wave packets is to be probed, an ability to vary the distance between the camera and the interaction region would be necessary. To obviate the need for physically moving anything, multiple accelerating zones could be established to vary the time needed for the wave packet to reach the detector.

Below, we calculate the ejection spectra for a coherent superposition of Rydberg states near $n = 50$. The Rydberg period of these states is 19 ps, which sets the upper limit for temporal resolution for observation of the dynamics. Clearly, the resolution and repetitive scan jitter of the streak camera must be less than this. This time scale also puts constraints on the size of the atomic ensemble (or more correctly the focused spot of the laser) used in the experiment as well as the ensemble temperature. Consider, for example, two wave packets emitted at the same time from two atoms moving with the same velocity but separated by x_0, twice the focused beam radius (w_0). If the electrons from the two atoms are to arrive at the detector within, say, 10 ps of each other, so as to be considered as part of the same wave packet, then $x_0/\bar{k} \lesssim 10$ ps. For 1-eV electrons, for example, a beam diameter of no more than 6 μm can be tolerated. Since the atoms are moving relative to each other, there will be a Doppler spread to the wave packets. The magnitude of this spread will be $t_{transit} \Delta k/\bar{k}$, where $t_{transit}$ is the transit time to the entrance aperture of the camera (or more correctly the time it takes the electron to reach the end of the acceleration region) and Δk is the thermal spread of atomic velocities. To achieve a spread of 10 ps or less, a maximum time of $\bar{k} \times 10$ ps$/\Delta k$ is required. In the case of a heavy atom like Ba, the ratio $\Delta k/\bar{k}$ at room temperature is approximately 2.7×10^{-5}, leading to a maximum transit time of about 37 ns corresponding to a detector distance of 2.2 cm for 1-eV electrons. This time, of course, can be increased if the motion along the detection direction were reduced. With a transverse temperature of 3 K, for example, the transit time and detector distance will increase by a factor of 10. Finally, highest precision measurements nearly devoid of motional and spatial perturbations would require ultracold atoms and very tight focusing of the laser pulse.

VI. RESULTS FOR BA

In this section, the results from several different calculations for Ba are presented. All of the calculations are for wave packets centered near the $5d_{5/2} n\ell$ states with $n = 50$.

The Rydberg period for the wave packet is ~ 19 ps. At this energy the channels attached to the $6s$ threshold and the $5d_{3/2}$ threshold are open. The $6pn\ell$ channels are closed but do not give any perturbing Rydberg states near the energies of the wave packets. The electrons that are ejected into the continuum leaving the ion in the $5d_{3/2}$ state can be distinguished from those leaving the ion in the $6s$ state by the delay in the time of arrival at a detector at macroscopic distances. The dispersion in the continuum attached to the $5d_{3/2}$ would prevent useful measurements of the wave packets so all of the calculations will focus on the $6s$ channel. The frequency spread of the laser is the same for all of the calculations giving electron wave packets that initially have 2.4 ps full width at half maximum. The only differences between the calculations will be in the initial quantum state and the position of the detector.

Barium was chosen for these calculations because it seems to be the most promising atom from an experimental and theoretical perspective. The transition frequencies in Ba are favorable for certain types of lasers. The large mass of the Ba nucleus will reduce the spreading of the ejected electron's wave packet arising from the Doppler effect; this would allow the experiment to proceed at higher temperatures. The photoionization spectrum of Ba has been well reproduced in R-matrix calculations [20,21]. The dipole matrix elements in Eq. (16) have been checked, where possible, by using them to calculate photoionization cross sections that could be compared with experiment.

A model potential similar to that used by Greene and Aymar was utilized with an R-matrix program to calculate the short-range dipole matrix elements and K matrices in LS coupling. All of the calculations included $6s$, $7s$, $8s$, $6p$, $7p$, $8p$, $5d$, $6d$, $7d$, $4f$, $5f$, $6f$, $5g$, $6g$, and $7g$ channels. The $6s$, $6p$, and $5d$ channels were open or weakly closed in the calculation with all of the other channels strongly closed. The R-matrix box was 20 a.u. The LS-coupled parameters were transformed into the jQ-coupled parameters through a frame transformation [27,25]. The energy-dependent dipole matrix elements were generated using MQDT with the experimental threshold energies. A much higher accuracy in the resonance positions and interactions results when the experimental thresholds are used.

The photoionization cross section generated from the energy-dependent dipole matrix elements agreed very well with the previous calculations and experiments for excitation from the $6s^2$ ground state. This indicates a high level of accuracy for the dipole matrix elements and the calculated final state dynamics. We do not know of any previous results to compare with for excitation from the $6p^2\ ^3P_J$ excited states. The results for excitation from the excited states are not as accurate as those for excitation from the ground state because the $6p^2\ ^3P$ states have more correlation than the ground state and they are closer to the threshold. This introduces some inaccuracy in the dipole matrix elements although the calculated final state dynamics will be accurate. The calculations will be for the $J_I=0$ and $J_I=2$, $M_I=0$ states since these states can be excited by a two photon transition using linearly polarized laser light. The details of the calculations may not be accurate but the major trends should be correct.
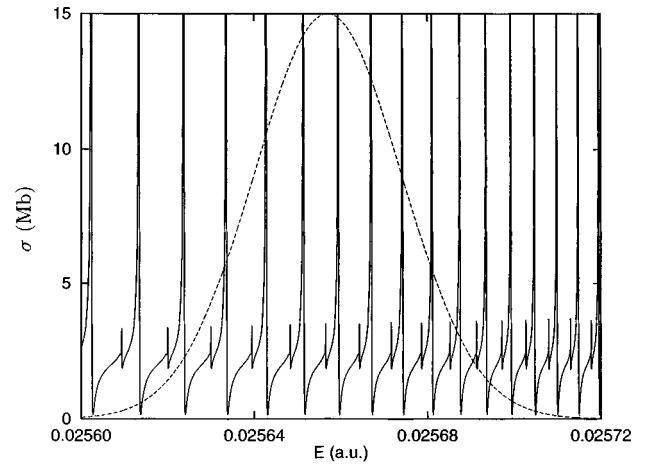

FIG. 1. Solid line: Infinite resolution partial photoionization cross section (from the $6s^2$ initial state leaving the ion in the $6s$ state) as a function of the ejected electron's energy. Dashed line: Proportional to $\mathcal{F}(E+E_{TH}-E_I-\omega)$ which corresponds to a laser field that generates an initial electron wave packet with a 2.4 ps full width at half maximum.

A. Excitation from the $6s^2$ state

The results for wave packets generated from laser excitation from the $6s^2$ ground state are described in this section. The partial photoionization cross section (leaving Ba$^+$ in the $6s$ state) as a function of the ejected electron energy is presented in Fig. 1. The dotted line in this figure is proportional to $\mathcal{F}(E+E_{TH}-E_I-\omega)$ where the total energy is $E+E_{TH}$ and $\omega=0.21716$ a.u. giving a photon wavelength of 209.8 nm. This wavelength could be generated by tripling a picosecond dye radiation at 629.4 nm. The calculations clearly demonstrate the cresting of the wave packets as well as two effects related to the angular distribution.

The initial state has $J_I=0$ and even parity. The final states must have $J=1$ and odd parity. The LS-coupled channels in the R-matrix calculation are $^1P^o$—$6s\varepsilon p$, $5dnp$, $5dnf$, $6pns$, and $6pnd$; $^3P^o$—$6s\varepsilon p$, $5dnp$, $5dnf$, $6pns$, and $6pnd$; $^3D^o$—$5dnp$, $5dnf$, and $6pnd$. The dipole matrix elements are only nonzero between states with the same total spin in LS coupling. For this calculation, the dipole matrix elements to the $^3P^o$ and $^3D^o$ channels are zero. In the MQDT calculation in jQ coupling, the 13 channels are $(6s_{1/2}0)\varepsilon p$ (this notation means the core state is $6s_{1/2}$, $Q=0$, and the continuum wave has $\ell=1$), $(6s_{1/2}1)\varepsilon p$, $(5d_{3/2}1)\varepsilon p$, $(5d_{3/2}2)\varepsilon p$, $(5d_{3/2}2)\varepsilon f$, $(5d_{5/2}2)np$, $(5d_{5/2}2)nf$, $(5d_{5/2}3)nf$, $(6p_{1/2}1)ns$, $(6p_{1/2}1)nd$, $(6p_{3/2}1)ns$, $(6p_{3/2}1)nd$, and $(6p_{3/2}2)nd$. Note, there are three Rydberg series attached to the $5d_{5/2}$ threshold. As mentioned in an earlier section, there are no perturbing Rydberg states attached to the $6p$ thresholds that fall near the range of interest although these channels are included in the calculation.

In Fig. 2, the temporal cross section is plotted for a distance of 1.9×10^6 a.u. $=10^{-2}$ cm from the atom. In all of the plots of the temporal cross section, the zero of time has been shifted so the full width of the direct ionization wave packet is visible. The electron wave packets in the continuum have not substantially dispersed at this distance. The temporal cross section parallel to the laser polarization is shown in
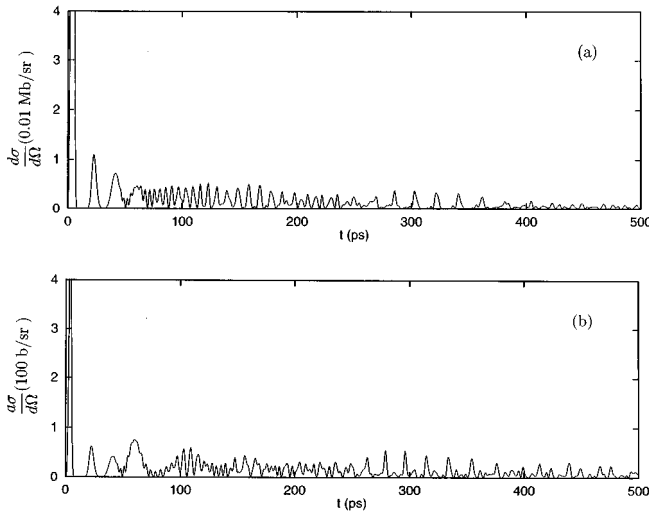
FIG. 2. (a) Temporal cross section parallel to the laser polarization at a distance of 10^{-2} cm. (b) Temporal cross section perpendicular to the laser polarization at a distance of 10^{-2} cm. In all of the temporal cross section plots, the zero of time has been shifted so the full width of the direct ionization pulse is visible. Only the direct ionization pulse and the 1–3 revolution pulses are distinguishable at this distance. Note the beating in (b) giving minima near 80 and 140 ps. Also note that near 300 ps where the Rydberg wave packet has completely revived, the main peaks in (a) are not at the same time as the main peaks in (b).
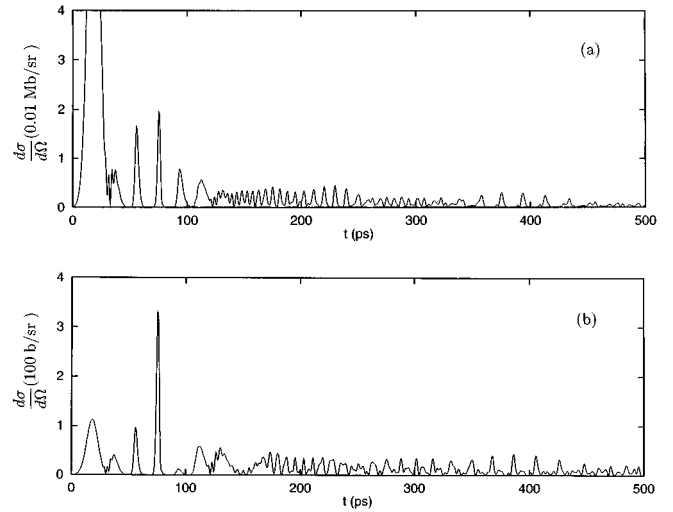
FIG. 3. Same as Fig. 2 except at a distance of 1 cm. The reverse dispersion of the wave packets is clearly present, making the direct ionization pulse and the 1–5 revolution pulses distinguishable. The four revolution peak in (b) is strongly suppressed which is the origin of the minima in Fig. 2(b) near 80 ps.

Fig. 2(a); the temporal cross section perpendicular to the polarization is shown in Fig. 2(b). A quick comparison of the scales for the figures shows that the electrons are mainly ejected parallel to the laser polarization. This is not surprising because the initial state and the core state do not have angular momentum. The first peak at ~ 4 ps arises from the direct ionization of the atom. The peak near 23 ps arises from the electrons excited into the $5d_{5/2}n\ell$ channels that first move away from the core then return after a time $\tau_{\mathrm{Ryd}} = 19$ ps to the core at which point they scatter into the open channel. The peak near 42 ps arises from the electrons excited into the $5d_{5/2}n\ell$ channels making two Rydberg revolutions before scattering into the open channel. The packet near 61 ps arises from the electrons making three Rydberg revolutions before scattering into the open channels. The Rydberg wave packets disperse with time and the higher revolution packets are not distinguishable. The fractional revival of the Rydberg wave packet can be seen [28] including the complete revival near 300 ps (the full revival time will be $2\pi\bar{\nu}^4/3 = 315$ ps [29] later than the time of the direct ionization pulse). This figure demonstrates our assertion in the Introduction that the behavior of the Rydberg wave packet can be detected through the electrons naturally ejected from autoionizing states. Except for the direct ionization peak, all of the features in Fig. 2 have their counterpart in previous studies of radial Rydberg wave packets.

In Fig. 3, the temporal cross section is plotted for a distance of 1.9×10^8 a.u. $= 1$ cm from the atom. At this distance, there is substantial dispersion of the electron wave packets in the continuum. The temporal cross section parallel to the laser polarization is shown in Fig. 3(a); the temporal cross section perpendicular to the polarization is shown in Fig. 3(b). The only change from Figs. 2 is the larger distance

to the detector. The direct ionization packet has spread to the extent that it now slightly overlaps the one revolution Rydberg wave packet giving an interference between the two packets. This illustrates the beautiful quantum principle that initially distinct electron wave packets can be made to interfere with each other. These figures also demonstrate the cresting of the electron's wave packet due to the reverse dispersion. This effect arises because electron wave packets disperse (are chirped) in opposite directions in the continuum and in the Rydberg states. Rydberg wave packets disperse by having the low energy part of the packet move to the front of the pulse while the continuum electron disperses by having the low energy part of the packet move to the rear of the pulse. These two types of dispersion will cancel at the distance given by Eqs. (36) and (37). The one revolution peak crests at 0.36 cm, the two revolution peak crests at 0.72 cm, the three revolution peak crests at 1.08 cm, etc. A remarkable point emerges from comparing Figs. 2 and 3. Figure 3 clearly shows a five revolution packet although after $5\tau_{\mathrm{Ryd}}$ the Rydberg wave packet does not exist as a packet *on the atom*; it has completely dispersed covering all of the classically allowed region of space.

In Fig. 4, the temporal cross section is plotted for a distance of 3.8×10^8 a.u. $= 2$ cm with everything else the same. At this distance the direct ionization packet and the 1–4 revolution packets have dispersed to the extent that they strongly overlap and interfere with each other. The 5–9 revolution packets are clearly visible as distinct pulses between 100 and 200 ps. It may be debatable whether to say these packets arise from N revolutions of the Rydberg electron because the Rydberg wave packet at the atom has completely dispersed after three revolutions. An argument in favor of this language could be made on the basis of Eqs. (27) and (33) where the wave function can be obtained by an expansion in terms of the closed-closed part of the short-range S matrix. Each order of the expansion makes a separate wave packet and can be identified with a specific number of revolutions; the number of revolutions equals the number of
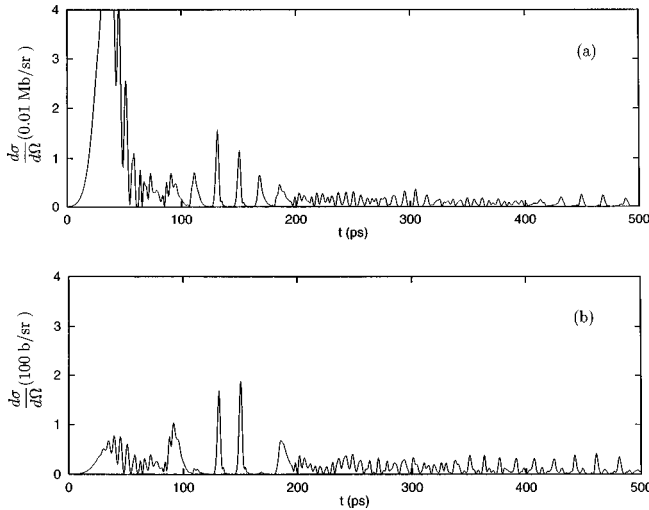
FIG. 4. Same as Fig. 2 except at a distance of 2 cm. The reverse dispersion of the wave packets is clearly visible, making the 4–8 revolution pulses distinguishable. The dispersion in the continuum causes the direct ionization pulse and the 1–3 revolution pulses to overlap each other, giving a jagged interference pattern up to 100 ps; in Fig. 2 these pulses were distinguishable. The four (near 110 ps) and seven (near 170 ps) revolution peaks are strongly suppressed in (b).

times S_{cc} appears in the amplitude of the packet minus 1. There are two interesting effects that arise from comparison of packets ejected parallel and perpendicular to the laser polarization.

One of the interesting effects relates to the wave packets near 300 ps, near the time at which the Rydberg wave packets have completely revived. The packets ejected in the parallel direction are peaked near the times 285 ps, 303 ps, 322 ps, 341 ps, and 362 ps. In the perpendicular direction, there is no sign of these packets. However, in the perpendicular direction there are packets near the times 279 ps, 296 ps, 314 ps, 334 ps, and 354 ps. There are peaks in the parallel direction at these times but they are much smaller than the ones at 285 ps, 303 ps, etc. Why is it that the main pulses ejected parallel to the laser polarization fall between the main pulses ejected perpendicular to the laser polarization? This mysterious situation is compounded by comparing Fig. 2 to Fig. 5 where the temporal cross section is shown for the distance 4 cm. Reverse dispersion causes the 11 revolution packet to crest near 4 cm. The wave packets near 300 ps (with the detector at 4 cm) are now detected at the same time in the parallel and the perpendicular direction. The reason for this strange behavior is unknown.

Another interesting effect is the apparent beating in the temporal cross section perpendicular to the laser polarization. In Fig. 2(b), it appears that the three revolution peak is too large compared to the one and two revolution peaks. There seems to be a sort of minimum in the temporal cross section near 80 ps, a broad maximum near 110 ps, and another minimum near 140 ps. The reason for this behavior is more apparent in Figs. 3(b) and 4(b). The four revolution packet and the seven revolution packet are almost completely suppressed. This behavior is striking because there is no hint of this behavior in the parallel direction. This erratic suppression of certain packets extends to higher revolutions
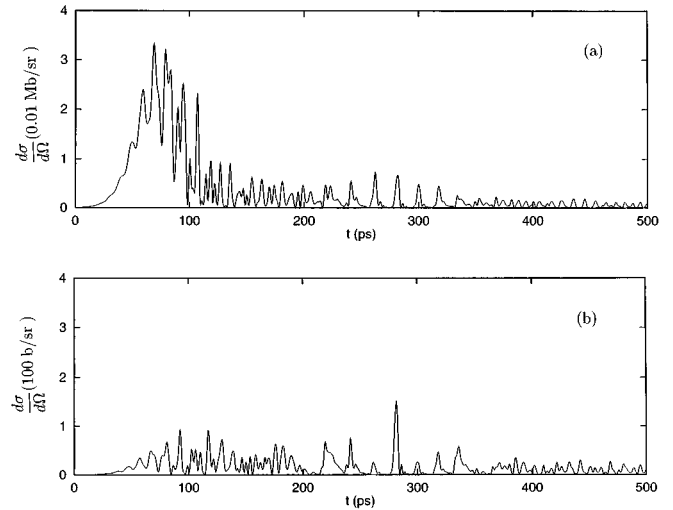
FIG. 5. Same as Fig. 2 except at a distance of 4 cm. The reverse dispersion of the wave packets is clearly visible, making the 9–13 revolution pulses distinguishable near 300 ps. Unlike in Fig. 2, the main pulses in (a) and (b) near 300 ps are at the same time.

as can be seen in Fig. 5(b) where the packets near 260 ps and 300 ps are almost completely suppressed.

The basic source of these suppressions probably is the number of closed channels. Each Rydberg revolution in channel j gives a phase to the packet of $2\pi(\nu_j - \ell_j - \mu_j)$. Since the quantum defects, μ_j, differ for the different channels, there will be some revolutions for which the amplitudes from the different channels add up constructively and some times when it adds up destructively. The details may be obscure but it seems probable this beating arises from interference between different but indistinguishable paths.

B. Excitation from the $6p^2\ {}^3P_0$ state

The ${}^3P_0$ state is 0.157 166 a.u. = 34 494 cm^{-1} above the $6s^2$ ground state. It is just below the ionization threshold. The partial photoionization cross section (leaving Ba$^+$ in the $6s$ state) as a function of the ejected electron's energy is presented in Fig. 6(a). The dotted line in this figure is proportional to $\mathcal{F}(E + E_{TH} - E_I - \omega)$ where $\omega = 0.059\ 99$ a.u. giving a photon wavelength of 759.5 nm near the peak of Ti:sapphire lasers. The energy-dependent β parameter

$$\frac{d\sigma}{d\Omega} = \frac{\sigma(E)}{4\pi}[1 + \beta(E)P_2(\cos\theta)] \qquad (40)$$

is presented in Fig. 6(b). An examination of Clebsch-Gordan coefficients gives $\beta = -1$ for the nonresonant part of the cross section. The nonresonant part of the cross section arises from the $6p^2\ {}^3P_0 + \hbar\omega \rightarrow 6s\varepsilon p\ {}^3P_1$. This is not obvious from the figure because the resonances are so broad it is difficult to disentangle the resonances from the background. The resonances with the most oscillator strength are mainly np in character. For this initial state the maximum of $\beta(E) \sim 1.1$.

The final state channels are the same as those in the preceding section. The only difference is the dipole matrix elements. In LS coupling the ${}^1P^o$ channels have dipole matrix elements equal to zero while the ${}^3P^o$ and ${}^3D^o$ channels have nonzero dipole matrix elements.
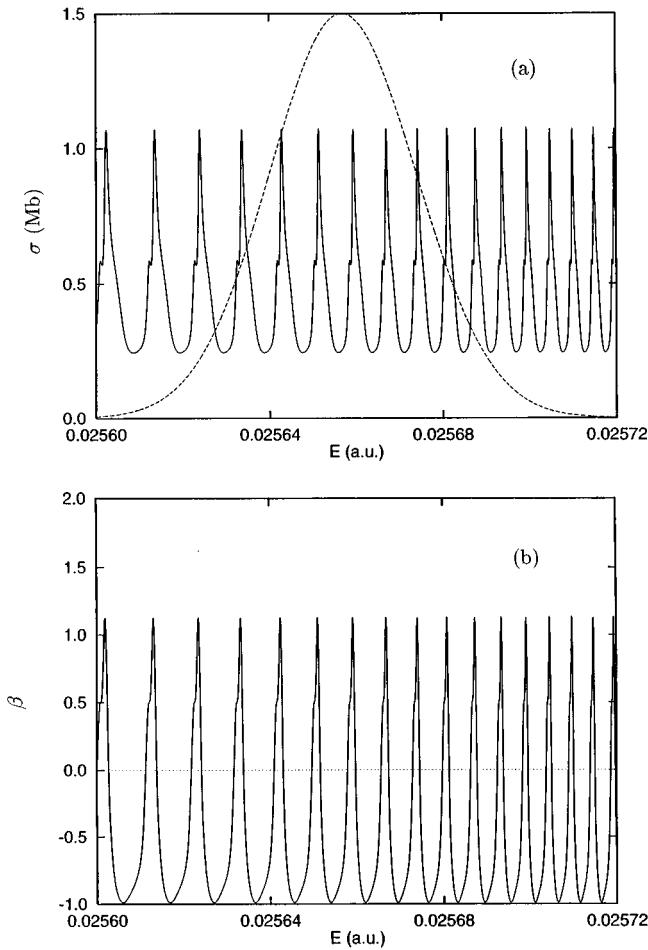
FIG. 6. (a) Same as Fig. 1 except for the initial state $6p^2\,{}^3P_0$. (b) The asymmetry parameter as a function of the ejected electron's energy. The nonresonant value of β for this initial state is -1.

FIG. 7. (a) The temporal cross section from the $6p^2\,{}^3P_0$ initial state parallel (solid line) and perpendicular (dashed line) to the laser polarization at 10^{-2} cm. (b) The temporal asymmetry parameter β. The direct ionization peak has $\beta = -1$. Note the steplike character of β when the packets do not overlap.

In Fig. 7(a), the temporal cross sections parallel (solid line) and perpendicular (dashed line) to the laser polarization are plotted for the distance of 1.9×10^6 a.u. $= 10^{-2}$ cm. There are relatively few wave packets generated because the $5d_{5/2}np$ states decay rapidly. It is clear from this figure that the direct ionization pulse is mainly ejected perpendicular to the laser polarization; the temporal cross section parallel to the laser polarization is essentially zero until ~ 15 ps. The temporal β parameter, Eq. (26), is plotted in Fig. 7(b). This parameter equals -1 until ~ 12 ps. This parameter exhibits a striking behavior. When a wave packet is completely distinguishable, the temporal β parameter is constant over that packet. This means there is an angular distribution associated with a packet.

This effect may be clearer in Fig. 8 where the temporal cross sections are plotted for a distance of 1 cm or in Fig. 9 where the distance is 2 cm. It appears that the direct ionization packet has a $\beta = -1$ and the N revolution packets have β's of $\beta_1 \sim 0.9$, $\beta_2 \sim 1.7$, $\beta_3 \sim 1.9$, $\beta_4 \sim 1.8$, $\beta_5 \sim 1.5$, and $\beta_6 \sim 1.0$. The remarkable aspect of these β values is that the energy-dependent β does not get larger than ~ 1.1. Much of the interference present in the energy-dependent β is not present in the temporal β, which may facilitate comparison between experiment and theory.
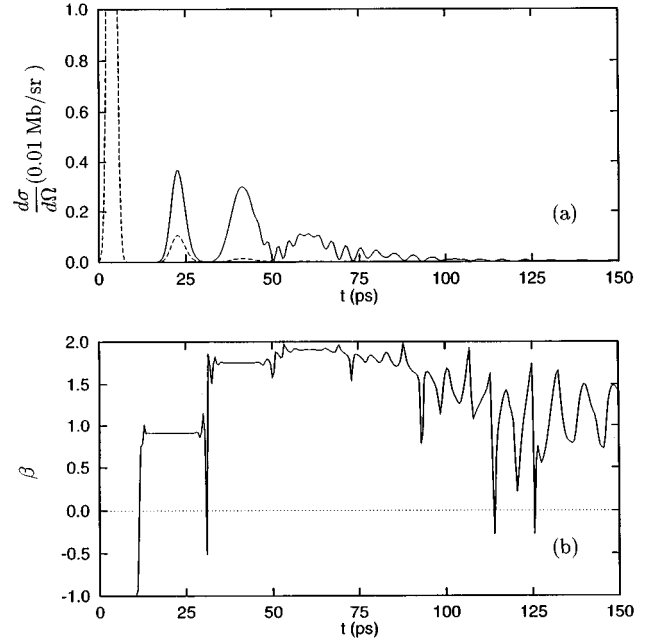
As discussed in Sec. IV D, this is the expected behavior

of the angular distribution of the ejected electrons. Nevertheless, it is a striking phenomenon. A comparison of Figs. 7(b) and 9(b) shows that the electron flux from 75 to 150 ps evolves from an erratic time dependence of the angular distribution in 7(b) to a simple steplike function in 9(b). Without knowing the basis for this effect, it would appear improbable that coherence in the electron flux could produce such an effect.

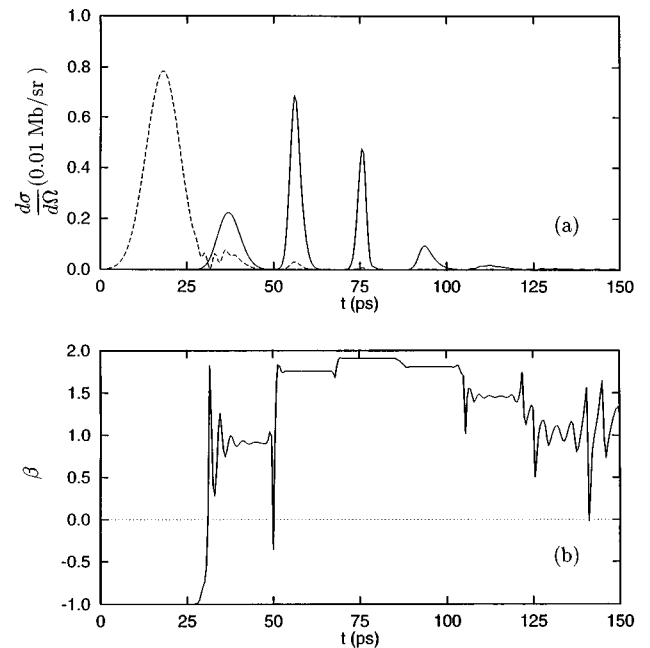The $^3P_2$ state is 0.162 283 a.u. = 35 617 cm^{-1} above the

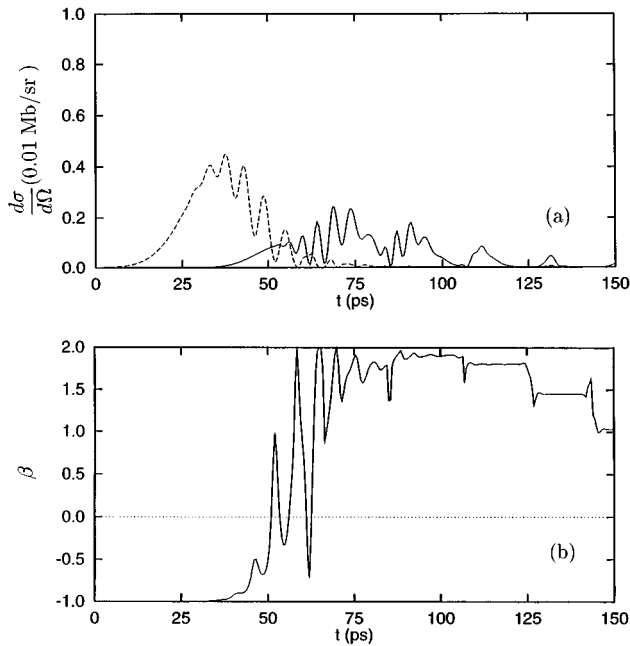FIG. 8. Same as Fig. 7 except at the distance 1 cm.

FIG. 9. Same as Fig. 7 except at the distance 2 cm.

$6s^2$ ground state. It is just below the ionization threshold and is another state that may be easy to utilize in an experiment. We performed several calculations for this state and found all of the main effects discussed above. There is a final interesting effect that is only present when this is the initial state. There is a long time trend in the ejected electron flux: the ejection of electrons perpendicular to the laser polarization becomes relatively less likely with time. We find an exponential decay of flux ejected perpendicular to the laser with a half-life of ~50 ps. The flux ejected parallel to the polarization has a half-life >200 ps. The short half-life perpendicular to the laser field indicates that it may be only np Rydberg states that are contributing to this process. That the different directions have different half-lives is a very striking result.

VII. DISCUSSION AND SPECULATION

In this paper, we have presented the theoretical results for the temporal detection of electrons ejected from autoionizing Rydberg wave packets. This development included the derivation of the wave function and the definition of a parameter, the temporal cross section. We analyzed the time dependence of the wave function at macroscopic distances from the atom and elucidated the angular dependence of the ejected wave packets. A prospective experimental arrangement has been described which should be able to resolve features on a picosecond time scale in the electron current.

Another purpose of this paper was to provide calculations for a specific atom. This provides a demonstration of several interesting effects that can be observed even for the simplest system. In all of the calculations, Ba was excited to $5d_{5/2}n\ell$ autoionizing states with $n \sim 50$. This is a simple region of energy because the Rydberg states near this energy are not perturbed by other Rydberg series. Even this simple system displayed several interesting effects. The wave packet cresting and the interference between initially distinguish-

able wave packets should be observable for this system. The complete revival wave packets may emerge at different times in different directions. Each wave packet has a specific angular distribution if it is distinguishable. The angular distribution for each wave packet varies in a smooth and systematic manner. The rate of electron ejection may depend on the direction with respect to the laser polarization.

We believe this to be a very promising field, ripe with unexplored possibilities. The most ideal target for these studies would be the autoionizing Rydberg states between the lowest ^2S and ^2D limits of the heavy alkaline earths Ca, Sr, and Ba. The most intriguing transition involves two photon excitation from the ns^2 ground state to the $np^2\ ^3P_J$ excited states. Photoionization out of the ^3P_J state to energies just below the $(n-1)d$ thresholds should give electron packets that are measurable. How will the dynamics be enriched in the presence of perturbing autoionizing states? We plan to explore many of these opportunities in future work, but we would like to briefly mention some of them here.

(1) One of the interesting aspects of the proposed experiment is the interference between initially distinguishable wave packets and the segregation of initially indistinguishable packets (what we have called cresting of the autoionizing wave packets). This effect can be observed because of the dispersion of the wave packets in the continuum. In many ways, this effect is analogous to the experiment performed by Noel and Stroud [30] where they made two separate electron wave packets in potassium with two laser pulses and probed the interference between the packets with a third laser pulse. The interference or segregation of wave packets is an interesting quantum effect which probes the frontier between quantum and classical physics.

(2) For photoionization from an unpolarized initial state by linear polarized light, the radial flux of electrons at a distance r and angle θ with respect to the laser polarization has the form of Eq. (26). How will β depend on t? The β for the initial pulse has the value of the nonresonant background in an infinite resolution experiment. The subsequent pulses from the autoionizing packets might all have the same value of β or β might change drastically from packet to packet. In the case we explored in this paper, the β varied in a systematic manner from packet to packet. In the infinite resolution experiments, β changes drastically when the photon is at a resonance energy; but that β arises from the *interference* between direct and resonance ionization. The direct and autoionizing packets do not necessarily overlap in our proposed experiment so the β for the autoionizing packets may only arise from the resonance contribution.

(3) The signature of some physical effects may be more apparent in the time-dependent flux than in the infinite resolution cross section. For example, the effect of the spin-orbit interaction on the cross section can be accurately incorporated into the infinite resolution cross section using a frame transformation on the MQDT parameters. However, the resulting spectrum can be very complicated with few features that are easily understandable. Perhaps the physics underlying the frame transformation (the precession of the core's spin and orbital angular momentum about the total angular momentum) will give a specific type of time dependence to $\beta(t)$ or $\sigma_0^{av}(r,t)$ in Eq. (26).

(4) The short-range scattering matrix, dipole matrix ele-

ments, and threshold energies determine both the infinite resolution cross section and time-dependent flux in the pulsed laser experiment. It may be possible to extract some aspects of these parameters in a very simple manner from the time-dependent flux. As an example, in Eq. (33) the size of the first pulse compared to the autoionizing pulses depends on these parameters in a way that is not very sensitive to the parameters. The time-dependent flux can provide information that will complement the infinite resolution experiments.

(5) There will be interesting effects arising from multi-channel interactions and coherences. For example, Henle *et al.* [10] found that a resonance from one channel can interact with resonances in a second channel in such a way that the resonances in the second channel are almost equally spaced; the dispersion of the wave packet in the second channel was essentially reduced to zero. As another example, we have found a model case where the resonances in one channel caused a variation in absorption into a second channel in

such a way that the dipole matrix elements to some Rydberg levels were greatly reduced. This also reduced the dispersion of the wave packet. We have not yet explored the details of these odd systems.

In conclusion, we feel this physical system demonstrates many interesting features. There does not appear to be any fundamental limitation that would prevent the proposed measurements.

[1] J.A. Yeazell and C.R. Stroud, Phys. Rev. Lett. **60**, 1494 (1988).

[2] A. ten Wolde, L.D. Noordam, H.G. Muller, A. Lagendijk, and H.B. van Linden van den Heuvell, Phys. Rev. Lett. **61**, 2099 (1988).

[3] J.A. Yeazell, M. Mallalieu, J. Parker, and C.R. Stroud, Phys. Rev. A **40**, 5040 (1989).

[4] J.A. Yeazell, M. Mallalieu, and C.R. Stroud, Phys. Rev. Lett. **64**, 2007 (1990).

[5] J.A. Yeazell and C.R. Stroud, Phys. Rev. A **43**, 5153 (1991).

[6] X. Wang and W.E. Cooke, Phys. Rev. Lett. **67**, 1496 (1991); Phys. Rev. A **46**, 4347 (1992).

[7] B. Broers, J.F. Christian, J.H. Hoogeraad, W.J. van der Zande, H.B. van Linden van den Heuvell, and L.D. Noordam, Phys. Rev. Lett. **71**, 344 (1993); B. Broers, J.F. Christian, and H.B. van Linden van den Heuvell, Phys. Rev. A **49**, 2498 (1994).

[8] H.H. Fielding, J. Wals, W.J. van der Zande, and H.B. van Linden van den Heuvell, Phys. Rev. A **51**, 611 (1995).

[9] G. Alber and P. Zoller, Phys. Rep. **199**, 231 (1991).

[10] W.A. Henle, H. Ritsch, and P. Zoller, Phys. Rev. A **36**, 683 (1987).

[11] H.H. Fielding, J. Phys. B **27**, 5883 (1994).

[12] L.D. Noordam, D.I. Duncan, and T.F. Gallagher, Phys. Rev. A **45**, 4734 (1992).

[13] R.R. Jones, C.S. Raman, D.W. Schumacher, and P.H. Bucksbaum, Phys. Rev. Lett. **71**, 2575 (1993).

[14] G.M. Lankhuijzen and L.D. Noordam, Phys. Rev. Lett. **76**, 1784 (1995).

[15] U. Fano and A.R.P. Rau, *Atomic Collisions and Spectra* (Academic, Orlando, 1986); M. J. Seaton, Rep. Prog. Phys. **46**, 167 (1983).

[16] C.H. Greene and L. Kim, Phys. Rev. A **36**, 2706 (1987).

[17] L. Kim and C.H. Greene, Phys. Rev. A **36**, 4272 (1987).

[18] M. Aymar, J. Phys. B **20**, 6507 (1987).

[19] M. Aymar and J.M. Lecomte, J. Phys. B **22**, 223 (1989).

[20] M. Aymar, J. Phys. B **23**, 2697 (1990).

[21] C.H. Greene and M. Aymar, Phys. Rev. A **44**, 1773 (1991), and references therein.

[22] C.H. Greene and Ch. Jungen, Adv. At. Mol. Phys. **21**, 51 (1985).

[23] A.F. Starace, in *Corpuscles and Radiation in Matter I*, Encyclopedia of Physics Vol. XXXI (Springer-Verlag, Berlin, 1982).

[24] R.D. Cowan, *Theory of Atomic Structure and Spectra* (University of California Press, Berkeley, 1981).

[25] M.D. Lindsay, C.-J. Dai, L.-T. Cai, T.F. Gallagher, F. Robicheaux, and C.H. Greene, Phys. Rev. A **46**, 3789 (1992).

[26] A.R. Edmonds, *Angular Momentum in Quantum Mechanics* (Princeton University Press, Princeton, NJ, 1968).

[27] A.R.P. Rau and U. Fano, Phys. Rev. A **4**, 1751 (1971); C.M. Lee and K.T. Lu, *ibid.* **8**, 1241 (1973).

[28] I. Sh. Averbukh and N.F. Perel'man, Zh. Eksp. Teor. Fiz. **96**, 818 (1989) [Sov. Phys. JETP **69**, 3 (1989)].

[29] J. Parker and C.R. Stroud, Phys. Rev. Lett. **56**, 716 (1986).

[30] M.W. Noel and C.R. Stroud, Phys. Rev. Lett. **75**, 1252 (1995).